The *S* receiver functions: synthetics and data example

Xiaohui Yuan, Rainer Kind,* Xueqing Li and Rongjiang Wang

GeoForschungsZentrum Potsdam, Telegrafenberg, 14473 *Potsdam, Germany. E-mail: yuan@gfz-potsdam.de*

SUMMARY

Recently, the *S* receiver function method has been successfully developed to identify upper mantle interfaces. *S* receiver functions have the advantage of being free of *S*-wave multiple reflections and can be more suitable than *P* receiver functions for studying mantle lithosphere. However, because of specific ray geometry and interference of diverse phases, the *S* receiver function method has some technical difficulties and limitations. We use synthetic seismograms to demonstrate the feasibility and limitations of *S* receiver functions for studying mantle structures. Full-wavefield seismograms were calculated using the reflectivity method and processed to generate synthetic *S* receiver functions for *S*, *SKS* and *ScS* waves. Results show that *S* receiver functions can be obtained from waveforms of *S*, *SKS* and *ScS* waves. The synthetic *S* receiver functions for these incident waves show *S*-to-*P* converted phases at all discontinuities in the crust and upper mantle. Useful ranges of epicentral distances for calculation of *S* receiver functions are: 55°–85° for *S*, >85° for *SKS* and 50°–75° for *ScS* waves. We apply both the *S* and *P* receiver function methods to data recorded at broadband station YKW3 in Northwest Canada. The study shows that there is significant agreement among different receiver function methods, and demonstrates the usefulness of *S* receiver functions for imaging the mantle lithosphere.

Key words: reflectivity method, *S* receiver function, *S* wave, *ScS* wave, *SKS* wave, synthetic seismogram.

INTRODUCTION

Mode conversions of teleseismic body waves provide an important means to investigate the nature of seismic discontinuities in the crust and mantle. Observations of the *P*-to-*S* and *S*-to-*P* conversions have been made for years (Båth & Stefánsson 1966; Phinney 1964). The *P*-to-*S* converted waves can be isolated from the *P* wave by receiver function analysis (Langston 1977; Vinnik 1977). Over the last decade, the receiver function method has become a standard tool to investigate crust and mantle structures (e.g. Kind *et al.* 2002; Bostock *et al.* 2002). The receiver function algorithm is composed of mainly two steps: first, a coordinate rotation isolates the *P*-to-*S* converted waves from the *P* wave; and second, deconvolution removes the source-site complications and the propagation effects. Further processing steps like moveout correction, common-conversion-point stack and migration enable us to construct receiver function profiles for dense seismic arrays (Duecker & Sheehan 1997; Yuan *et al.* 1997; Bostock *et al.* 2001; Kind *et al.* 2002).

While most previous studies have focussed on analysing *P*-to-*S* conversions by the *P* receiver function method, the study of *S*-to-*P* conversions is still at the experimental stage because of a series of

technical challenges. Since *S* waves (*S*, *SKS*, *ScS*) are not the first arrivals, they sometimes arrive within the *P*-wave coda. *S* waves are characterized by lower frequencies than *P* waves, resulting in a lower spatial resolution. The *S*-to-*P* converted waves cannot be observed over all teleseismic distances as they sometimes occur at critical incidence angles. Most previous studies have focussed on the identification of *S*-to-*P* converted waves from long-period seismograms. Polarity analysis was often used to distinguish the *S*-to-*P* converted waves from the *S* waves. The objects of these studies include the crust-mantle boundary (Båth & Stefánsson 1966; Smith 1970; Jordan & Frazer 1975; Burdick & Langston 1977), the base of the lithosphere (Sacks & Snoke 1977; Sacks *et al.* 1979; Snoke *et al.* 1977; Bock 1991) and the discontinuities in the mantle transition zone (Farber & Müller 1980, 1984; Bock & Kind 1991).

Recently, receiver function analysis (coordinate rotation and deconvolution) was also applied to *S* waves to isolate the *S*-to-*P* converted phases from the incident *S* phases (Farra & Vinnik 2000; Vinnik & Farra 2002; Vinnik *et al.* 2003, 2004). This initiated the *S* receiver function method, which is closely related to the conventional *P* receiver function. The method has been improved by introducing stacks of individual *S* receiver functions by geographic locations of the piercing points, with emphasis on mapping the lithosphere–asthenosphere boundary (Li *et al.* 2004; Kumar *et al.* 2005a,b,c).

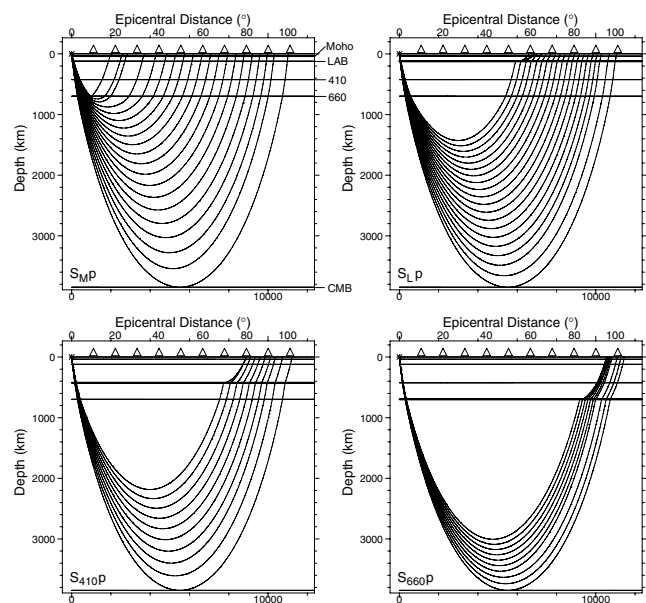*Also at: Freie Universität Berlin, Malteserstr. 74-100, 12249 Berlin, Germany.

Velocity (km s^{-1})
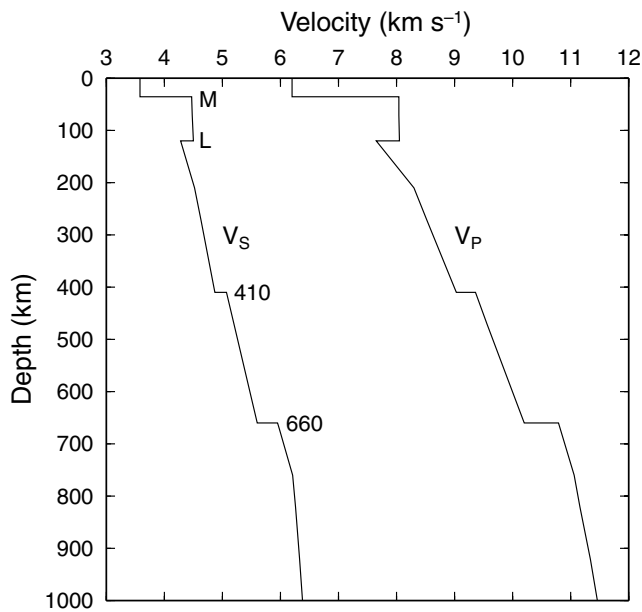
Figure 1. Model of *P*-and *S*-wave velocities for calculation of synthetic seismograms. Only the upper part of the model down to a depth of 1000 km is shown here. It contains four discontinuities, Moho, LAB, the 410- and 660-km discontinuities. The lower part of the model is the same as the IASP91 model. Compared with the IASP91 model, the crust has been simplified to a single 35-km-thick layer.

The *S* receiver function method has the advantage of being free of multiple reflections, making it suitable for studying seismic discontinuities at lithospheric and asthenospheric depths. However, because of the specific ray geometry of the *S*-to-*P* converted waves, the use of *S* receiver function is limited to certain ranges of epicentral distances. This problem can be clearly illustrated by synthetic seismograms. Previous synthetic *S*-wave seismograms (Farber & Müller 1980, 1984; Bock 1994) were calculated at low frequency, and consequently addressed the conversions at the 410- and 660-km discontinuities. In this paper, we calculate high-frequency synthetic seismograms of *S*, *SKS* and *ScS* waves at teleseismic distances and process them to create *S* receiver functions. As a data example, we analysed and compared the *P* and *S* receiver functions of station YKW3 located in southern Slave craton, northwest Canada.

The Earth model used throughout the paper is a modified form of IASP91 (Kennett & Engdahl 1991). Fig. 1 shows the upper part of the model to a depth of 1000 km. The crust has been simplified to a single, 35-km-thick layer. A negative velocity jump of 5 per cent was introduced at 120-km depth to represent the lithosphere–asthenosphere boundary (LAB). We defined a first-order discontinuity for the base of the lithosphere, although the boundary is more likely a transition zone. The IASP91 model already includes the 410- and 660-km discontinuities in the mantle transition zone.

We follow the convention that *P* receiver function is for the receiver function dealing with *P*-to-*S* conversions and *S* receiver function for the receiver function dealing with *S*-to-*P* conversions from *S*, *SKS* and *ScS* waves. When we distinguish the specific type of the *P* and *S* receiver functions, we use *PRF*, *SRF*, *SKSRF* and *ScSRF*. *S*-to-*P* conversions at the Moho, LAB, 410- and 660-km discontinuities are denoted as S_Mp, S_Lp, $S_{410}p$ and $S_{660}p$ for the *SRF*, SKS_Mp, SKS_Lp, $SKS_{410}p$ and $SKS_{660}p$ for the *SKSRF* and ScS_Mp, ScS_Lp, $ScS_{410}p$ and $ScS_{660}p$ for the *ScSRF*.


Figure 2. Possible ray paths of teleseismic *S*-to-*P* converted waves for the mantle *S* waves. The source is at the surface. Ray tracing was carried out for the *S* waves over entire teleseismic distances. Only paths of *S*-to-*P* conversions are shown in each subfigure. The thick horizontal lines mark the interfaces, where the *S*-to-*P* conversions occurred. Because of critical incidence, some paths of *S*-to-*P* converted waves do not exist at small distances.

TELESEISMIC *S*-TO-*P* CONVERSIONS

The incidence angle of an *S*-to-*P* converted wave is usually larger than that of the incident *S* wave. For the mantle *S* waves, critical incidence angles are present for the *S*-to-*P* conversions so that there are no conversions at certain epicentral distances. Fig. 2 shows all the possible ray paths of S_Mp, S_Lp, $S_{410}p$ and $S_{660}p$, calculated by a Gaussian beam ray tracing algorithm (Weber 1988; Davis & Henson 1993). *S*-to-*P* conversions at greater depths do not exist at short epicentral distances due to over-critical incidence. Only the S_Mp can be observed at all the distances. The S_Lp, $S_{410}p$ and $S_{660}p$ can only be observed at distances larger than approximately 60°, 80° and 95°, respectively. Because of scattering effects in the real Earth, these distance ranges are in practice slightly broader than the ones given by ray theory. From Fig. 2, observation of the 410- and 660-km discontinuities is possible only within a narrow range of epicentral distances with the mantle *S* waves. Other phases such as *SKS* and *ScS* can be used to observe these deeper discontinuities, as *SKS* and *ScS* waves travel more steeply to stations, so that critical incidence is avoided.

Fig. 3 shows the *S*–*P* transmission coefficients of the *S*-to-*P* conversions for the above discontinuities (Aki & Richards 1980). *S*-*P* transmission coefficients of Moho, and the 410- and 660-km discontinuities are negative, while the one for the LAB is positive. The absolute value of the transmission coefficients increases with increasing slowness (decreasing epicentral distance). The horizontal axis of slowness and epicentral distance refers to the reference *S* and *SKS* waves and may differ from those of the *S*-to-*P* converted waves at near-critical incidence angles. *S* waves have a slowness range of 8.3–13.4 s deg^{-1} with the distance range of 55°–105°. The slowness range of *SKS* waves at distances 85°–115° is 3.8–6.4 s deg^{-1}. Note that the transmission coefficients of the 410- and 660-km discontinuities for the *S* waves only exist at small
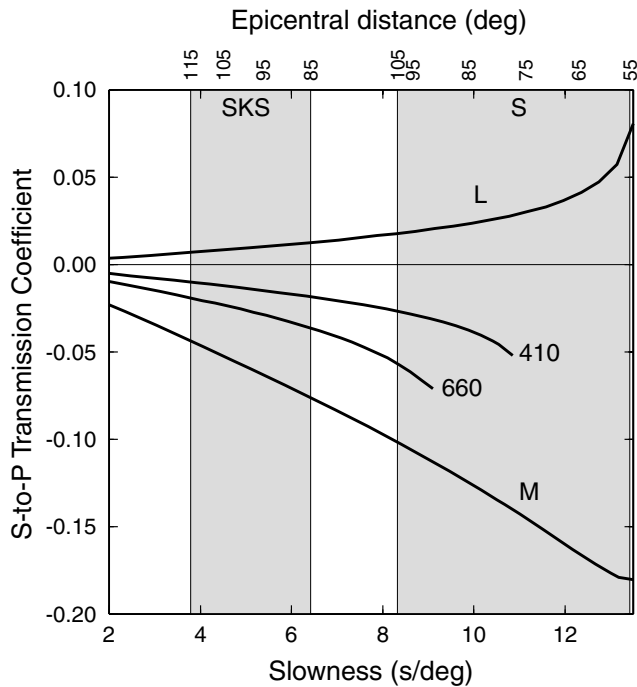
Figure 3. Conversion coefficients for *S*-to-*P* conversions at the Moho, LAB, and the 410- and 660-km discontinuities (Aki & Richards 1980). The model is shown in Fig. 1. Horizontal axis of slowness and epicentral distance refer to the incident *S* and *SKS* waves and may differ from those of the *S*-to-*P* converted waves at near-critical incidence angles. Shaded zones are the slowness/distance ranges of *S* and *SKS* waves, respectively.

slowness (large distances). *S* waves generally have larger transmission coefficients than *SKS* waves.

FULL-WAVEFIELD SYNTHETIC SEISMOGRAMS

Full-wavefield seismograms were calculated using the reflectivity method (Wang 1999). The algorithm solved the numerical difficulty in the original Thomson–Haskell propagation by adopting a numerical procedure that makes the fundamental displacement vector *in situ* orthonormal. The method is efficient and stable for a wide range of applications from calculation of static deformation to generating high-frequency seismograms (Wang 1999). The Earth flattening approximation (Mueller 1977) is used to account for the Earth's curvature.

Fig. 4 shows the record sections of three-component synthetic seismograms for a dislocation point source. The model is shown in Fig. 1. A vertical dip-slip point source with strike perpendicular to the azimuth between the source and receiver was placed close to the surface (at a depth of 10 m). The source mechanism used here can only generate *P* and *SV* waves, so there is no motion on the transverse component. The synthetic seismograms have been calculated for a range of epicentral distances from 40° to 120° with 1° station interval and a time window of 2000 s for 4096 samples with time reduction by a slowness of 10 s deg^{-1}. Seismic waves whose turning points are shallower than 400-km depth were excluded. This filtered out much of the surface waves that would be otherwise the dominant phases in the seismogram sections. Time-domain aliasing was suppressed by the use of complex frequencies (Kind & Seidl 1982).
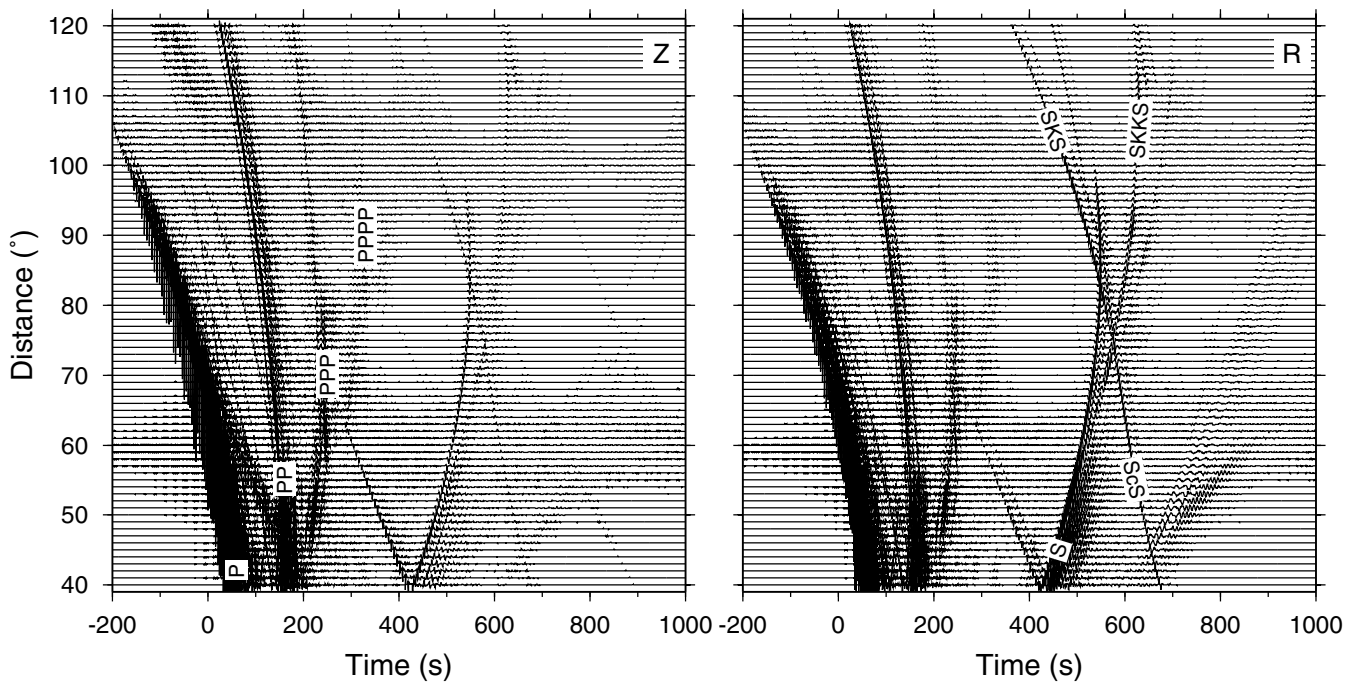
Figure 4. Vertical (a) and radial (b) component full-response seismograms calculated by the reflectivity method for the model shown in Fig. 1. Time is reduced by a slowness of 10 s deg^{-1}. Main phases are labelled on the corresponding components.
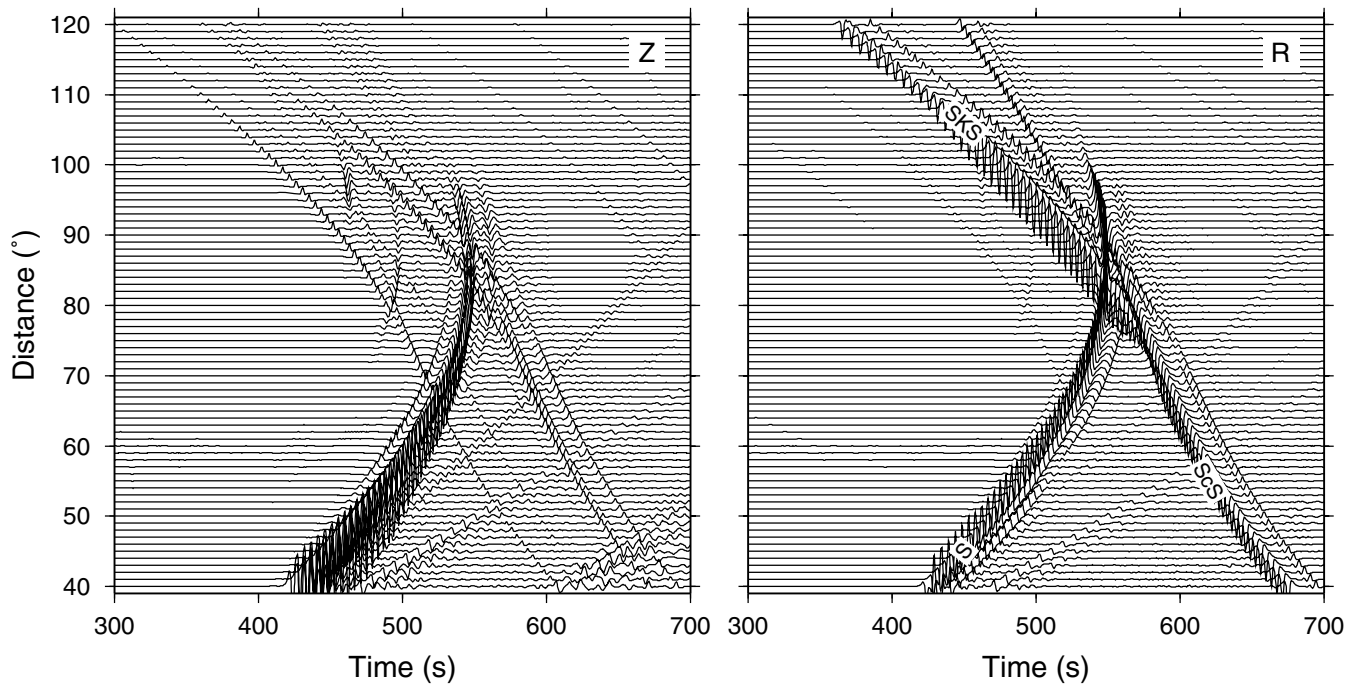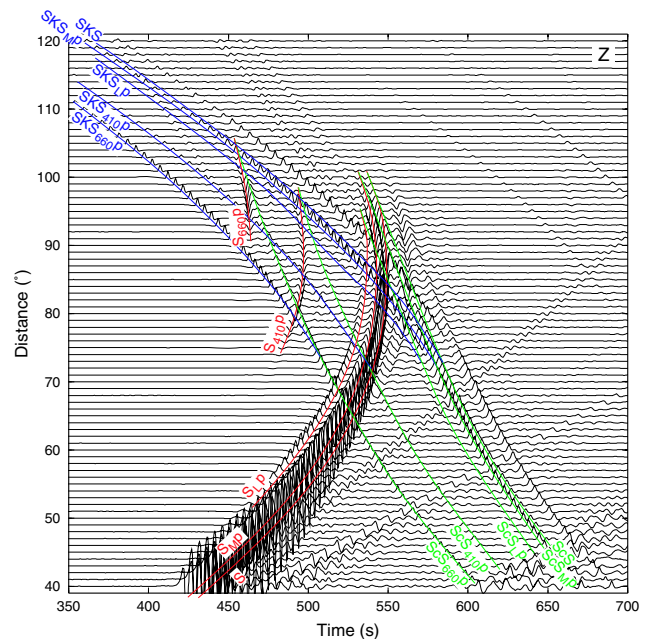
Figure 5. Vertical and radial component synthetic *S*-wave seismograms calculated by the reflectivity method. The main mantle *P* waves as well as the surface reflections are removed from the wavefield by a partial solution approach. The amplitudes of the vertical component are amplified by a factor of 5. Time is reduced by a slowness of 10 s deg^{-1}. Main phases of the S, *SKS* and *ScS* are labelled on the R component. A series of *S*-to-*P* converted phases can be clearly seen on the vertical component.

The vertical (Z) component seismograms are dominated by the mantle *P* waves as well as the multiple surface reflections such as *PP*, *PPP* and *PPPP* etc. The SV waves such as the *S*, *ScS*, *SKS* and *SKKS* waves are more prominent on the radial (R) component. The amplitude ratio between *P* and *S* waves depends on numerous factors, for example, source orientation and frequency content.

The *P*-wave multiple surface reflections may appear with significant amplitudes at times prior to *S*, causing interference with the *S*-to-*P* converted waves (Sacks *et al.* 1979; Bock 1994). This phenomenon can be important for the synthetic seismograms calculated with a 1-D model. Because of the lateral homogeneity and sharp interfaces in the model, there are many multiple reverberations in the synthetic seismograms. The weak *S*-to-*P* conversions could be masked by any types of multiple phases. In the real Earth, most of these multiples can be destructively correlated owing to lateral heterogeneity and, therefore, are sufficiently decayed. Here, we used a special technique to filter out all the disturbing *P* waves. The reflectivity code used here has an option for partial wavefield solution. We used the option that the downgoing *P* waves do not participate in the matrix propagation procedure and are, in this way, filtered out from the wave field. To show the receiver side *S*-to-*P* conversions, the upgoing *P* waves are untouched within the matrix propagation procedure. At the end, only the upgoing *S*-to-*P* converted waves along with the whole set of *S* waves will arrive at the receivers.

Fig. 5 is the resultant Z- and R-component seismograms, that is, with all the downgoing *P* waves filtered out. *S*, *SKS* and *ScS* phases are clearly seen on both the Z and R components. A series of converted waves from *S*, *SKS* and *ScS* waves at a number of discontinuities appear on the Z component as precursors to each corresponding reference phase. These converted phases are marked and labelled in Fig. 6. They are converted at discontinuities of Moho,

Figure 6. Vertical component synthetic *S*-wave seismograms with a time reduction by a slowness of 10 s deg^{-1}. The converted phases from S, *SKS* and ScS waves at Moho, LAB, the 410- and 660-km discontinuities are marked and labelled.

LAB, the 410- and 660-km discontinuities. Such conversions can be seen for all the triggering phases (*S*, *SKS* and *ScS*). The sign of the amplitudes depends on the sign of the velocity contrast of the discontinuities and the polarities of the triggering phases. It should be noted that the polarities of the precursors to *S* are different from
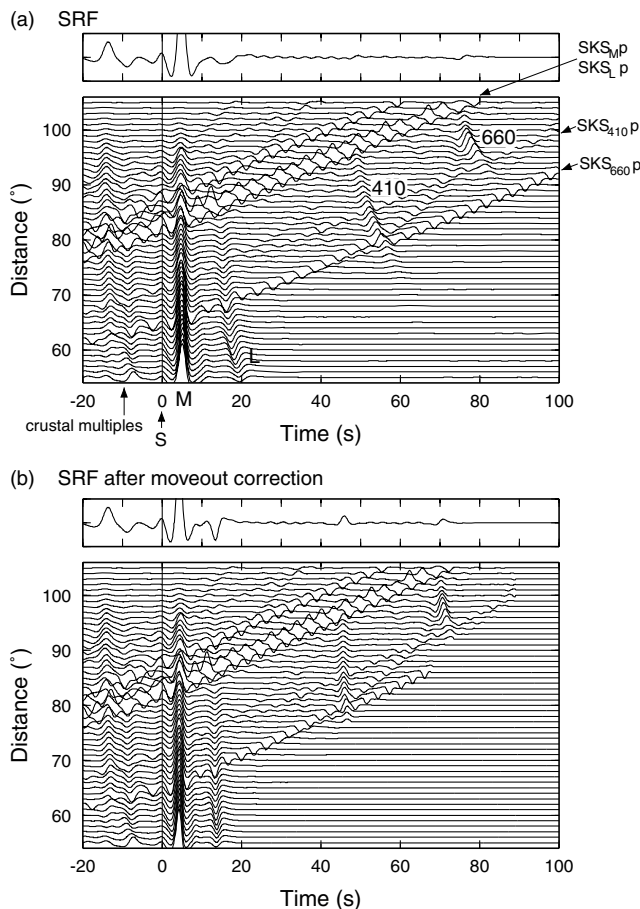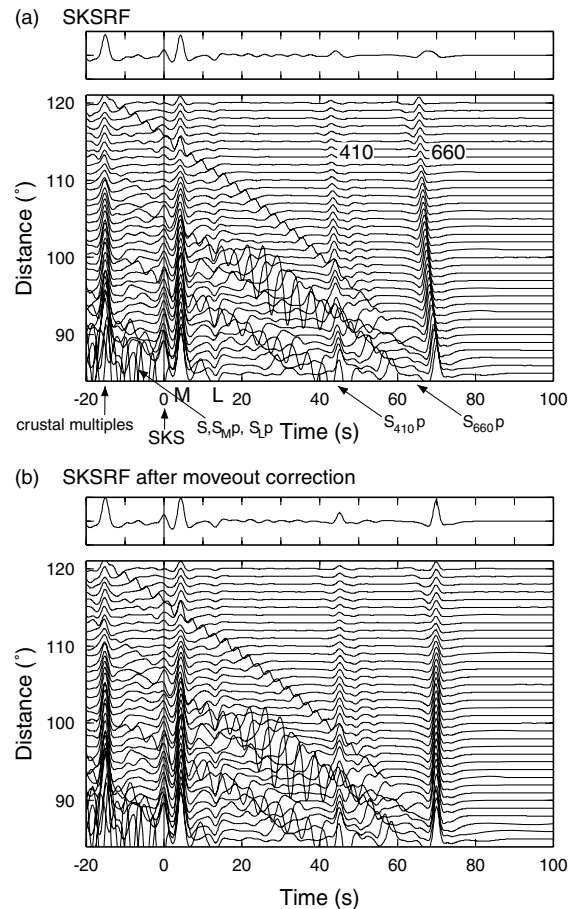
Figure 7. *S* receiver functions of *S* waves before (a) and after (b) moveout correction. The individual receiver functions are sorted by epicentral distances from 55° to 105°. The top panel is the summation trace. Converted phases are labelled in (a). The interfering phases from *SKS* waves are also marked in (a).

those of the precursors to *SKS* on the Z component, because the *S* and *SKS* have different signs on the R component.

S RECEIVER FUNCTIONS

We processed the synthetic data of *S*, *SKS* and *ScS* phases separately to generate *S* receiver functions for each phase. The processing steps are described as follows:

(1) Seismograms were aligned by the maximum amplitudes of each reference phase on the radial components and were cut 100 s before and 20 s after the corresponding reference phase. We reversed the time axis so that the *S*-to-*P* conversions have positive arrival times. For different reference phases (S, *SKS* and *ScS*), we selected different ranges of epicentral distances. For *S* phase, we selected seismograms corresponding to distances of 55°–105°. The diffracted *S* wave, Sdiff, is used as the reference phase for distances over 95°. Beyond 85° distance, *SKS* waves arrive before S. Fig. 7 shows a zoom on the *SRFs* at distances smaller than 105°. We later show that only distances smaller than 85° are adequate for the *S* receiver function analysis of the *S* phase. The distance ranges shown for *SKS* (Fig. 8) and *ScS* (Fig. 9) are 85°–120° and 45°–80°, respectively. At distances shorter than 50°, *ScS* strongly interferes with the mantle

Figure 8. *S* receiver functions of *SKS* waves before (a) and after (b) moveout correction. The individual receiver functions are sorted by epicentral distances from 85° to 120°. The top panel is the summation trace. Converted phases are labelled in (a). The interfering phases from *S* waves are also marked in (a).

SS waves, which is why these shorter distances are avoided in our calculation (Figs 4–6 and 9).

(2) The Z and R components of the mantle *S* phases are rotated into ray coordinate system L and Q components, where L and Q point to the *P* and *SV* wave polarization directions, respectively. The incidence angle for the rotation was determined by minimizing the amplitudes of Q components at *S* arrival times. Because the incidence of *SKS* waves is much steeper, we use the Z and R components for *SKS* without any rotation. We also use Z and R components for the *ScS* phase.

(3) The synthetic seismograms were calculated with an impulsive source time function. The source was placed at the surface to avoid a complex source signature. Deconvolution is therefore not necessary. The amplitudes of the *SKSRFs* are multiplied by −1 to account for the reversed polarity of the *SKS*. The resulting *S* receiver functions are plotted in Figs 7(a), 8(a) and 9(a). For field data, deconvolution is used for source equalization and the amplitudes should be adjusted relative to the reference phases.

(4) Moveout correction is applied to the *S* receiver functions to correct for the time dependence with epicentral distance (Figs 7b, 8b and 9b). A reference slowness of 6.4 s deg^{-1} and the IASP91 model are used for the moveout correction.

The resulting *S* receiver functions are shown in Figs 7–9. In *S* receiver functions, the primary *S*-to-*P* conversions are separated

(a)   ScSRF

(b)   ScSRF after moveout correction
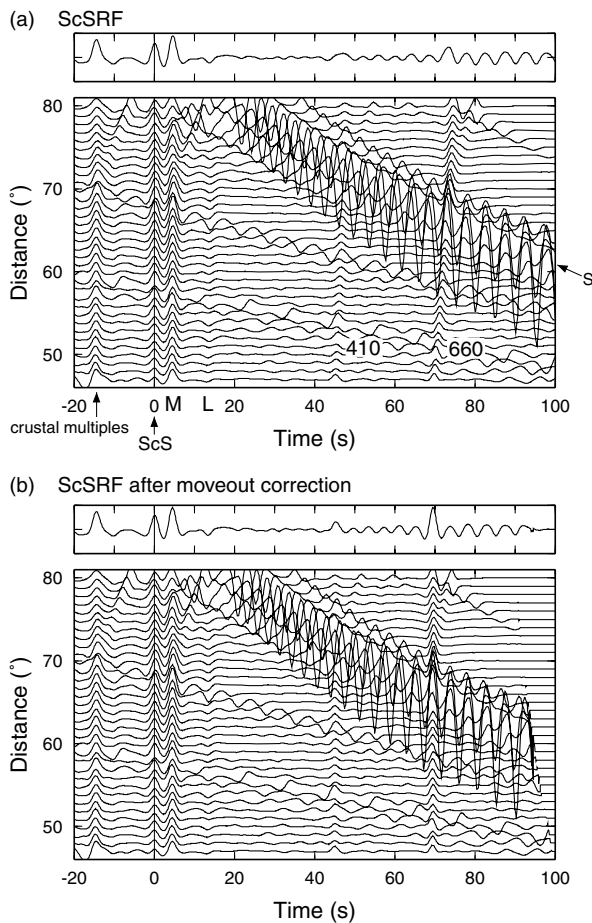
Figure 9. *S* receiver functions of *ScS* waves before (a) and after (b) moveout correction. The individual receiver functions are sorted by epicentral distances from 47° to 80°. The top panel is the summation trace. Converted phases are labelled in (a). The interfering phases from *S* waves are also marked in (a).

from the multiple reflections by the *S* arrivals. Crustal multiples can be clearly seen at negative time. These multiples may be used to give important constraint on the crustal thickness and the average Poisson's ratio (Owens & Zandt 1997). However, this subject is beyond the scope of this paper. We focus here on the primary conversions in the positive time range.

The *SRFs* clearly contain the conversions at Moho, LAB, the 410- and 660-km discontinuities (Fig. 7a), but they are observed at different epicentral distances. Moho is detected at almost all distances (55°–95°). The LAB can be seen at distances of 55°–80° with maximum amplitudes at 60°–70° distances. The 410-km discontinuity is observed only between 80° and 95°, and the 660-km discontinuity between 95° and 100°. Strong *SKS* waves interfere with the *SRFs*. At distances larger than 85°, the interpretation of the *S* receiver functions becomes problematic, because *SKS* waves arrive earlier than the mantle *S* waves. The useful distance range of *S* waves to detect the Moho and LAB should consequently be limited to 55–85°, estimated for a LAB depth of 120 km. The range varies with the LAB depth. It can be extended to shorter distances for a thinner lithosphere and should be limited to larger distances for a thicker lithosphere. In this range, the 660-km discontinuity cannot

be observed. The chance for observing the 410-km discontinuity is small.

Because of the effect of moveout, only Moho can be clearly seen in the simple summation trace (Fig. 7a). A moveout correction is therefore necessary to detect the LAB. We correct the arrival time of each data sample with a reference slowness of 6.4 s deg^{-1}. After the moveout correction, the converted phases are almost aligned and clearly have significant stacked amplitudes (Fig. 7b). We notice that in Fig. 7(b), the moveout for the 410- and 660-km discontinuities is not completely corrected, as both phases are inclined at small distances. This is due to the plane wave assumption used in the moveout correction, where the slowness of the converted wave is assumed to be the same as that of the reference phase. This assumption causes inaccuracy in the moveout correction. The problem is more serious for the conversions at deep interfaces, for example, the 410- and 660-km discontinuities, at near-critical incidence. It is, however, negligible for the Moho and LAB, which constitute the main targets of the *S* receiver functions.

Fig. 8 shows the *SKSRFs* before and after moveout correction. A few per cent of *SKS* amplitudes is seen at 0 s, especially at shorter distances, due to the use of the vertical rather than the L component. Although the conversion coefficients for *SKS* are smaller than for *S* (Fig. 3), the SKS_Mp, $SKS_{410}p$ and $SKS_{660}p$ are clear throughout the whole section. The SKS_Lp is somewhat weaker. At shorter distances, the SKS_Mp and SKS_Lp are masked by or interfered with a series of strong *S* waves and converted waves. The weak SKS_Lp may, however, not be a general characteristics of the *SKSRF*. The amplitude of *SKS* conversions depends on the source mechanism. The influence of the disturbing *S* waves is minimized for some sources that favour *SKS* waves. The 410- and 660-km discontinuities can be reliably identified with *SKS* receiver functions.

Similar as the *SKSRFs* (Fig. 8), the *ScS* receiver functions are also computed on the vertical component (Fig. 9). The remaining energy at 0 s can be removed if the vertical component is rotated to the component of *P* wave propagation direction. The *ScS* receiver functions are relatively noisy due to interference with *S* waves (Fig. 9). At short distances, the *ScS* waves interfere with mantle *SS* waves (see also Fig. 5). The useful range of epicentral distances is 50–75°, within which the reference *ScS* waveform can be extracted for deconvolution. The *S*-to-*P* conversions at shallower interfaces such as the Moho are clearly separated from the *S* waves over full range of useful distances. Deeper interfaces (the 410- and 660-km discontinuities) are more visible at shorter distances (50–65°).

Fig. 10(a) shows the *S* and *SKS* receiver functions together. The traces are sorted by slowness. The *SKSRF* has a slowness smaller than 6.5 s deg^{-1} and the *SRF* has a slowness greater than 8.0 s deg^{-1}. For demonstration purpose, we also plotted the *SRFs* for distances greater than 85° (slowness of 8–10 s deg^{-1}). For field data, the slowness range of 8–10 s deg^{-1} is not useful because of the interference of *S* and *SKS* phases. Only the Moho phase is visible in the summation trace before moveout correction. After moveout correction (Fig. 10b), all the converted phases are aligned in the receiver function section and become clearly visible in the summation. Similarly to the *P* receiver functions, the *S* receiver functions can also be displayed in depth section (Fig. 10c) by a simple back projection along the *S*-wave paths. The *SKSRFs* sample an area closer to the station, while the piercing points of the *SRFs* are farther away from the station. The apparent dipping of the reconstructed interfaces with the *SRF* data, especially the 660, is due to the plane wave assumption that is invalid at large slownesses. The effect can be of course easily corrected by a slowness correction.

(a) SRF+SKSRF

(b) SRF+SKSRF after moveout correction

(c) SRF+SKSRF depth section
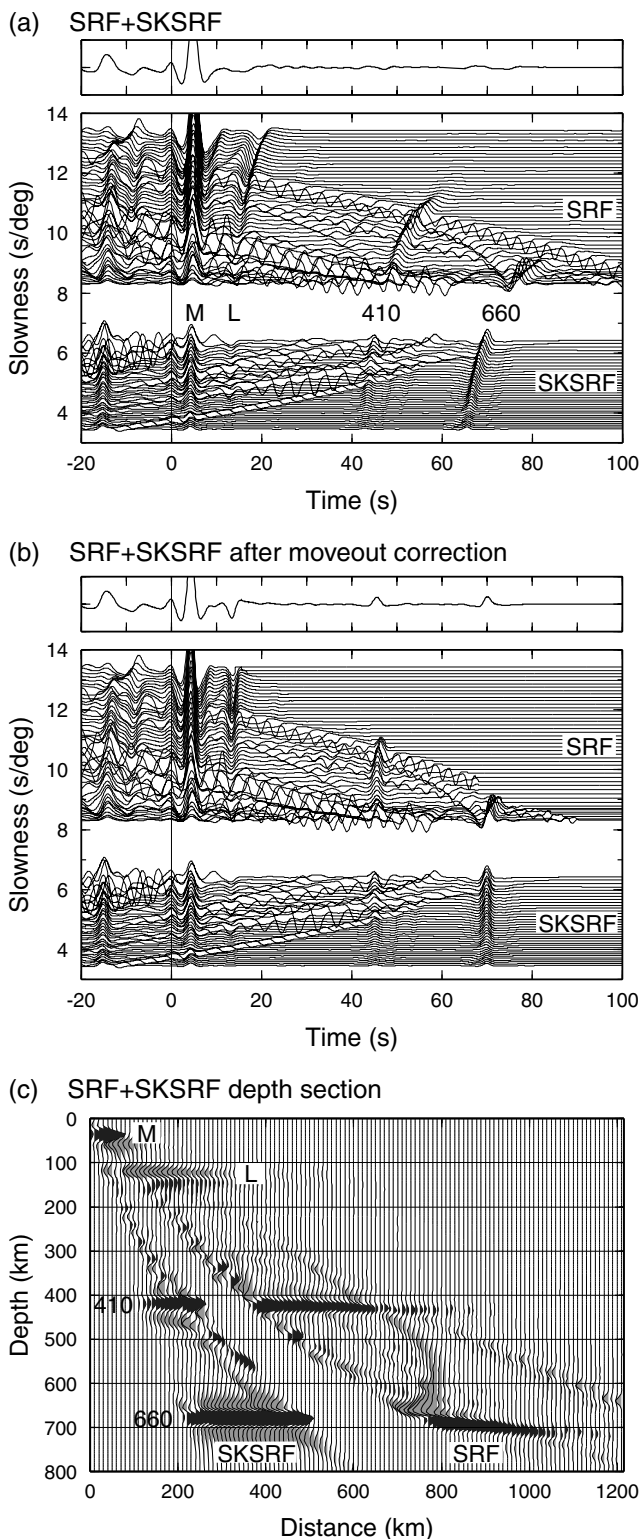
Figure 10. (a) Synthetic *S* receiver functions sorted by slowness. The slowness of *SKSRF* is less than 6.5 s deg^{-1} while the slowness of the *SRF* is larger than 8.0 s deg^{-1}. Major conversion phases are labelled. (b) same as (a) but for moveout corrected *S* receiver functions. A slowness of 6.4 s deg^{-1} and the IASP91 model are used as reference. (c) Depth section of the *S* receiver functions. The IASP91 model is used for the time-depth transformation. The piercing points of the *SKSRFs* are closer to the stations than those of the *SRFs*.

DATA EXAMPLE

To demonstrate the use of the *S* receiver functions with field data, we analysed teleseismic earthquake records at the broadband station YKW3 of the Yellowknife seismic array, located in southern Slave province, northwest Canada. The station was installed in late 1989 and has collected a large amount of data. The Slave province is one of the oldest Archaen cratons on Earth. Seismology has provided detailed information about the crust and upper mantle structure (e.g. Cook *et al.* 1999; Bostock 1998; Frederiksen *et al.* 2001). *P* receiver functions have revealed Moho and the 410- and 660-km discontinuities along with a series of complicated upper mantle structures underneath the station (Bostock 1998). The station is ideal to compare the *P* and *S* receiver functions. We compiled waveform data of *P*, *S* and *SKS* waves recorded at YKW3. We selected teleseismic earthquakes with magnitudes larger than 5.9 and epicentral distances of 35–95° for *P*, 55–85° for *S* and >85° for *SKS*. The *PRFs* were analysed in the way described by Yuan *et al.* (1997), consisting of mainly coordinate rotation into the *P-SV-SH* system and deconvolution of the *SV* and *SH* components by the *P* component. The analysis of the *SRF* and *SKSRF* is as described by Li *et al.* (2004) and Kumar *et al.* (2005a,b,c), and is somewhat different from the synthetic data processing. Here we briefly summarize the processing steps for generating *S* receiver functions. The ZNE-component seismograms of *S* and *SKS* waves are rotated firstly into the ZRT system with the back azimuth determined by locations of the receiver and earthquake. The ZRT components are further rotated into the *P-SV-SH* system with the incidence angle determined by minimizing the amplitudes at time of *S*/*SKS* arrival on the *P* component. Waveforms are visually selected to avoid the confusing of *S* and *SKS* phases. Data with strong interference of *S* and *SKS* are excluded. A window of *S*/*SKS* waves on the *SV* component is deconvolved from the *P* component for source equalization. For direct comparison with the *P* receiver functions, we need to reverse the time axis as well as the amplitudes of the *S* receiver functions. Moveout correction is then applied for all the *PRFs*, *SRFs* and *SKSRFs*, with a reference slowness of 6.4 s deg^{-1} and the IASP91 model as reference.

Fig. 11 shows the *P* and *S* receiver functions of station YKW3. The individual receiver functions are moveout corrected and sorted by the back azimuth. The summation trace is shown above each section. The number of *P* receiver functions is significantly larger than that of the *S* receiver functions, as the *P* receiver functions have a larger range of valid epicentral distances. *S* waves are usually noisier, so more *S* than *P* receiver functions are rejected owing to poor signal to noise ratio.

In the section of *PRFs* (Fig. 11a), the direct conversions of the Moho, and the 410- and 660-km discontinuities can be clearly followed in the individual traces throughout the whole section. Their arrival times are 4.2 s, 43.3 s and 67.3 s, respectively, very close to values obtained by earlier studies (Bostock & Cassidy 1997; Bostock 1998). At times 10–25 s, strong crustal multiple phases appear, effectively masking the possible direct *Ps* conversions from the mantle lithosphere at depth of 100–250 km. At ~8 s, between the direct Moho conversion and the Moho multiples, a phase with polarity reversal as a function of back azimuth can be identified in the individual traces. This phase was interpreted as an anisotropic layer in the uppermost mantle by Bostock (1998) by analysing the transverse component of *P* receiver functions. He also found a series of interfaces at depths of approximately 130, 200 and 350 km.
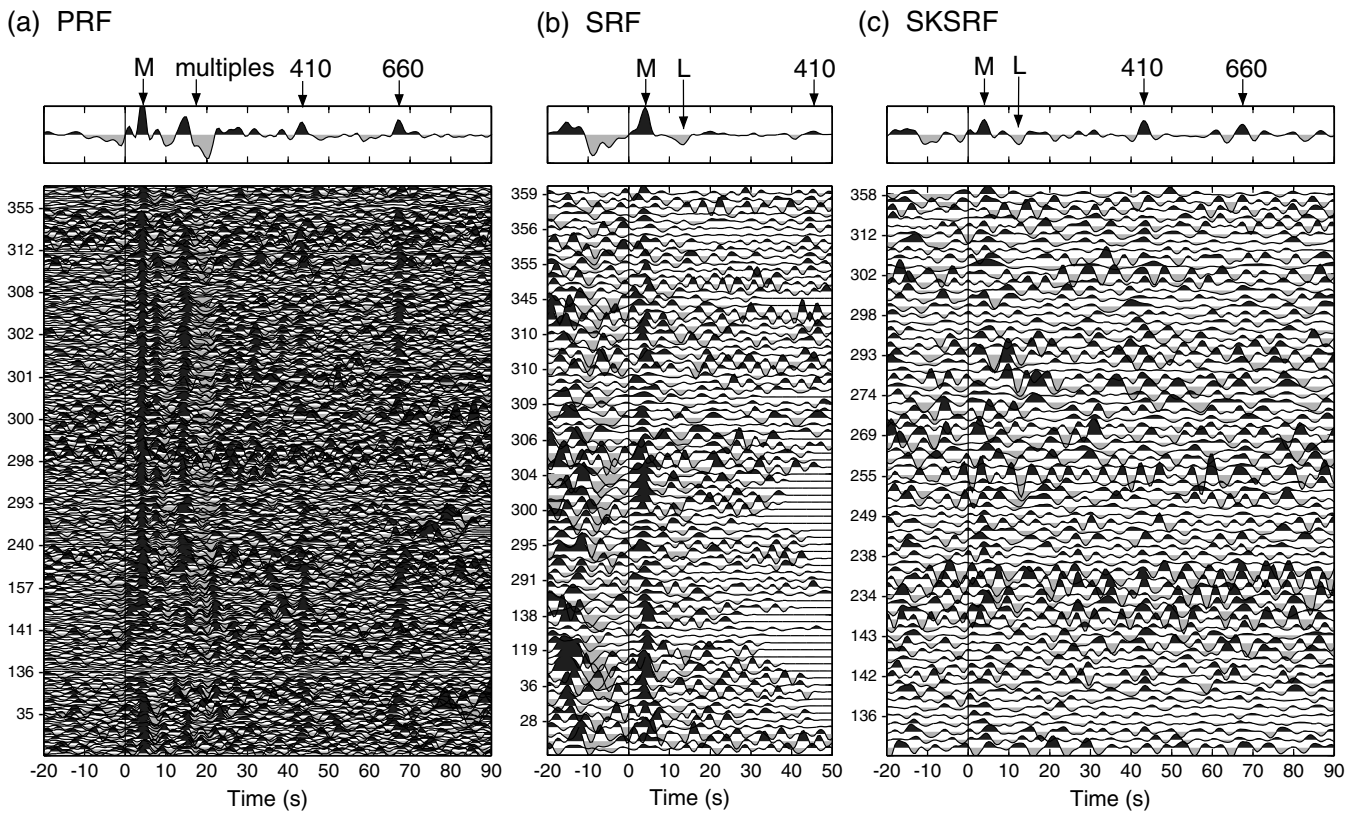
Figure 11. *PRFs*, *SRFs* and *SKSRFs* of station YKW3. The receiver functions are corrected for moveout with a reference slowness of 6.4 s deg^{-1} and a reference model of the IASP91. The number of the *PRFs* is more than 200, the numbers of the *SRFs* and *SKSRFs* are ∼80 each. A three-pole low-pass filter with corner frequency of 3 *S* is applied to all the data. Back azimuth values for some sample traces are labelled to the left of each trace. The summation trace is plotted above each receiver function section. Main conversion phases are labelled on the summation traces.
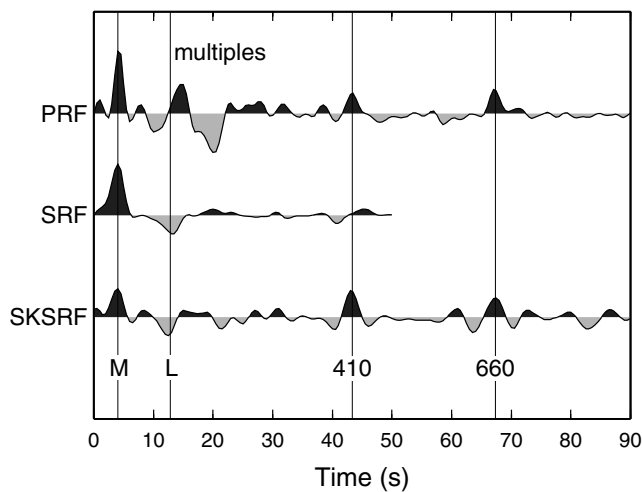
Figure 12. Summations of *PRFs*, *SRFs* and *SKSRFs* from Fig. 11 plotted together for direct comparison. The converted phases are marked with vertical lines. The crustal reverberation phases at time of 10–25 *S* in the *PRF* effectively mask the possible conversions of the mantle lithosphere in the *PRF*.

Because the *SRFs* are calculated for epicentral distances shorter than 85°, *S*-to-*P* conversions at the 660-km discontinuity are not available. Therefore, the section is plotted to 50 s (Fig. 11b). The *SRFs* clearly exhibit direct *S*-to-*P* conversions at Moho. At 12.8 s, a phase with negative amplitudes (L) can be identified. This phase

represents a relatively sharp boundary at a depth of ∼120 km with a lower shear-wave velocity below it. It could not simply be interpreted as the base of the lithosphere, as a more than 200-km-thick lithospheric root underneath the Slave craton was found by seismic tomography (Mégnin & Romanowicz 2000; Frederiksen *et al.* 2001). Earlier receiver function study also revealed a mantle interface at similar depth beneath the station (Bostock 1998) and interpreted it as compositional layering within the mantle lithosphere. The interface might coincide with a high electrical conductivity layer at the similar depth found in the central Slave craton by a magnetotelluric survey (Jones *et al.* 2003). The converted phase at the 410-km discontinuity, although weak, can be clearly seen in the individual traces.

All the discontinuities discussed above can be observed with *S*-to-*P* conversions from *SKS* waves (Fig. 11c). Although the individual traces have a relatively higher noise level, all the converted phases show up in the summation trace.

The summation traces of the *PRFs*, *SRFs* and *SKSRFs* are plotted together in Fig. 12 for a direct comparison. There is a very good agreement among different techniques. The Moho conversions observed with *PRF*, *SRF* and *SKSRF*, appear at 4.2 s, corresponding to a depth of 34 km using the IASP91 reference velocities. The 410- and 660-km discontinuities are also located at the same times by *PRF* and *SKSRF*. The time delay of the $S_{410}p$ in the *SRF* is caused by an insufficient moveout correction due to the plane wave assumption for the moveout correction. The low-velocity lithospheric interface (L) can be clearly identified in the *SRF* and *SKSRF*. Strong crustal reverberations dominate the time window of 10–25 s in the *PRF*,

precluding the *PRF* as a useful tool to detect the discontinuities at depth of the lithospheric upper mantle.

CONCLUSION

The *S* receiver function method is an useful complementary tool to the conventional *P* receiver function method. The *S* receiver function analyses the *S*-to-*P* converted waves at seismic discontinuities in the crust and mantle beneath the stations. The direct *S*-to-*P* converted waves arrive at the station earlier than the incident *S* wave, thus are naturally separated from the *S*-wave multiple reverberations that appear later than the *S* arrival, making the method suitable for investigating the mantle structure at lithospheric and asthenospheric depths. In the case that strong near-surface interfaces (e.g. the 2–3-km-thick ice sheet in central Greenland) exist and produce significant reverberations strong enough to mask the direct *P*-to-*S* conversions of the Moho in the *P* receiver functions, the *S* receiver functions are useful to observe the Moho (Kumar *et al.*, 2005d). The *S*-to-*P* converted waves do not split along the way to the station in an anisotropic medium, thus the complication of the shear-wave birefringence in the *P* receiver functions caused by seismic anisotropy is avoided in the *S* receiver functions. There are two more differences between the *P* and *S* receiver functions. The *S*-to-*P* conversions arrive earlier than the incident *S* wave, while the *P*-to-*S* conversions arrive later than the incident *P* wave. The transmission coefficient of an *S*-to-*P* conversion has different sign as that of a *P*-to-*S* conversion. It is convenient to reverse the amplitude sign and to swap the time axis for the *S* receiver functions for a comparison with the *P* receiver functions.

Theoretical calculation of seismograms show that the *S* receiver functions can be obtained from waveforms of *S*, *SKS* and *ScS* waves (Figs 7–9). The useful range of epicentral distances for the mantle *S* waves is $<85°$. The lower distance limit depends on the depth of the target of interest. For *S*-to-*P* conversions at discontinuities within the mantle lithosphere, the range is limited to $>55–60°$. The 410 km discontinuity can be observed within $75–85°$. Observation of the *S*-to-*P* conversions at the 660-km discontinuity with the mantle *S* waves is not possible. An adjustment in the moveout correction for the $S_{410}p$ is needed to correct for the plain wave assumption. The *SKS* waves are useful for epicentral distances $>85°$. They can be used for imaging all the crustal and upper mantle conversions. The *ScS* waves are useful for epicentral distances about $50–75°$. In this range, the *ScS* waves arrive between the mantle *S* and *SS* arrivals. Depending on the target discontinuities, the range must be adjusted. For example, for targeting the 660-km discontinuity, ranges of $65–70°$ should be removed because of the severe interference with the mantle *S* waves. At epicentral distances of $80–90°$, *S*, *SKS*, *SKKS* and *ScS* waves all arrive at similar times (see Fig. 5). Care must be taken while visually inspecting seismograms to avoid any contamination among different phases.

P and *S* receiver functions are calculated for station YKW3, located near Yellowknife in southern Slave province, northwest Canada (Figs 11 and 12). There is a good agreement among different techniques. The Moho conversions observed with *PRF*, *SRF* and *SKSRF*, appear at the same time, 4.2 s, at a slowness of 6.4 s deg^{-1}, corresponding to a depth of 34 km, estimated with the IASP91 model. The 410- and 660-km discontinuities are identical with both *PRF* and *SKSRF*, arriving at times of 43.3 s and 67.3 s, respectively. The time delay of the $S_{410}p$ is caused by an insufficient moveout correction due to the plain wave assumption. A low-velocity layer in the upper mantle at 120 km depth can be clearly identified in the

SRF and *SKSRF*. Strong crustal reverberations dominate the time window of 10–25 s in the PRF, masking the possible conversions at lithospheric depths in the *P* receiver functions.

REFERENCES

Aki, K. & Richards, P.G., 1980. *Quantitative Seismology: Theory and Methods*, W. H. Freeman and Company, San Francisco, pp. 133–155.

Båth, M. & Stefánnson, R., 1966. S-P conversion at base of the crust, *Ann. Geofis.,* **19,** 119–130.

Bock, G., 1991. Long-period S to P converted waves and the onset of partial melting beneath Oahu, Hawaii, *Geophys. Res. Lett.,* **18,** 869–872.

Bock, G., 1994. Multiples as precursors to S, SKS and ScS, *Geophys. J. Int.,* **119,** 421–427.

Bock, G. & Kind, R., 1991. A global study of *S*-to-*P* and P-to-S conversions from the upper mantle transition zone, *Geophys. J. Int.,* **107,** 117–129.

Bostock, M.G., 1998. Mantle stratigraphy and evolution of the Slave province, *J. geophys. Res.,* **103,** 21 183–21 200.

Bostock, M.G. & Cassidy, J.F., 1997. Upper mantle stratigraphy beneath the southern Slave craton, *Can. J. Earth Sci.,* **34,** 577–587.

Bostock, M.G., Rondenay, S. & Shragge, J., 2001. Multiparameter two-dimensional inversion of scattered teleseismic body waves; 1, Theory for oblique incidence, *J. geophys. Res.,* **106,** 30 771–30 782.

Bostock, M.G., Hyndman, R.D., Rondeny, S. & Peacock, S.M., 2002. An inverted continental Moho and serpentinization of the forearc mantle, *Nature,* **417,** 536–538.

Burdick, L.J. & Langston, C.A., 1977. Modeling crustal structure through the use of converted phases in teleseismic body-wave forms, *Bull. seism. Soc. Am.,* **67,** 677–691.

Cook, F.A., van der Velden, A.J., Hall, K.W. & Roberts, B.J., 1999. Frozen subduction in Canada's Northwest Territories: Lithoprobe deep lithospheric reflection profiling of the western Canadian shield, *Tectonics,* **18,** 1–24.

Davis, J.P. & Henson, I.H., 1993. User's guide to Xgbm: An X-windows system to compute Gaussian beam synthetic seismograms, Report TGAL-93–02, Teledyne Geotech Alexandria Laboratories.

Duecker, K.G. & Sheehan, A.F., 1997. Mantle discontinuity structure from midpoint stacks of converted P to S waves across the Yellowstone hotspot track, *J. geophys. Res.,* **102,** 8313–8327.

Farber, S. & Müller, G., 1980. Sp phases from the transition zone between the upper and lower mantle, *Bull. seism. Soc. Am.,* **70,** 487–508.

Farber, S. & Müller, G., 1984. Converted phases from the mantle transition zone observed at European stations, *J. Geophys.,* **54,** 183–194.

Farra, V. & Vinnik, L., 2000. Upper mantle stratification by P and S receiver functions, *Geophys. J. Int.,* **141,** 699–712.

Frederiksen, A.W., Bostock, M.G. & Cassidy, J.F., 2001. S-wave velocity structure of the Canadian upper mantle, *Phys. Earth planet. Inter.,* **124,** 175–191.

Jones, A.G., Lezaeta, P., Ferguson, I.J., Chave, A.D., Evans, R.L., Garcia, X. & Spratt, J., 2003. The electrical structure of the Slave craton, *Lithos,* **71,** 505–527.

Jordan, T.H. & Frazer, L.N., 1975. Crustal and upper mantle structure from Sp phases, *J. geophys. Res.,* **80,** 1504–1518.

Kennett, B.L.N. & Engdahl, E.R., 1991. Travel times for global earthquake location and phase identification, *Geophys. J. Int.,* **105,** 429–465.

Kind, R. & Seidl, D., 1982. Analysis of broadband seismograms from the Chile-Peru area, *Bull. seism. Soc. Am.,* **72,** 2131–2145.

Kind, R. et al, 2002. Seismic images of the crust and upper mantle beneath Tibet: evidence For eurasian plate subduction, *Science,* **298,** 1219–1221.

Kumar, P., Yuan, X., Kind, R. & Kosarev, G., 2005a. The lithosphere–asthenosphere boundary in the Tien Shan-Karakoram Region from S receiver functions—evidence for continental subduction, *Geophys. Res. Lett.,* **32,** L07305, doi:10.1029/2004GL022291.

Kumar, P. *et al.*, 2005b. The lithosphere–asthenosphere boundary in the north west Atlantic region, *Earth planet. Sci. Lett.,* **236,** 249–257.

Kumar, P., Yuan, X., Kind, R. & Ni, J., 2005c. Imaging the colliding Indian and Asian continental lithospheres beneath Tibet, *J. geophys. Res.,* submitted.

Kumar, P., Kind, R., Priestley, K. & Dahl-Jensen, T., 2005d. Crustal structures of Iceland and Greenland from receiver function studies, *J. geophys. Res.,* submitted.

Langston, C.A., 1977. Corvallis, Oregon, crustal and upper mantle structure from teleseismic P and S waves, *Bull. seism. Soc. Am.,* **67,** 713–724.

Li, X., Kind, R., Yuan, X., Wölbern, I. & Hanka, W., 2004. Rejuvenation of the lithosphere by the Hawaiian plume, *Nature,* **427,** 827–829.

Mégnin, Ch. & Romanowicz, B., 2000. The three-dimensional shear velocity structure of the mantle from inversion of body, surface and higher-mode waveforms, *Geophys. J. Int.,* **143,** 709–728.

Mueller, G., 1977. Earth-flattering approximation for body waves derived from geometric ray theory—improvements, corrections and range of applicability, *J. Geophys.,* **42,** 429–436.

Owens, T.J. & Zandt, G., 1997. Implications of crustal properly variations for models of Tibetan Plateau evolution, *Nature,* **387,** 37–43.

Phinney, R.A., 1964. Structure of the Earth's crust from spectral behavior of long-period body waves, *J. geophys. Res.,* **69,** 2997–3017.

Sacks, I.S. & Snoke, J.A., 1977. The use of converted phases to infer the depth of the lithosphere–asthenosphere boundary beneath South America, *J. geophys. Res.,* **82,** 2011–2017.

Sacks, I.S., Snoke, J.A. & Husebye, E.S., 1979. Lithosphere thickness beneath the Baltic shield, *Tectonophysics,* **56,** 101–110.

Snoke, J.A., Sacks, I.S. & Okada, H., 1977. Determination of the subducting lithosphere boundary by use of converted phases, *Bull. seism. Soc. Am.,* **67,** 1051–1060.

Smith, W.D., 1970. S to P conversion as an aid to crustal studies, *Geophys. J.,* **19,** 513–519.

Vinnik, L.P., 1977. Detection of waves converted from P to SV in the mantle, *Phys. Earth planet. Int.,* **15,** 39–45.

Vinnik, L. & Farra, V., 2002. Subcratonic low-velocity layer and flood basalts, *Geophys. Res. Lett.,* **29,** 1049, doi:10.1029/2001GL014064.

Vinnik, L., Kumar, M.R., Kind, R. & Farra, V., 2003. Super-deep low-velocity layer beneath the Arabian plate, *Geophys. Res. Lett.,* **30,** 1415, doi:10.1029/2002GL016590.

Vinnik, L., Farra, V. & Kind, R., 2004 Deep structure of the Afro-Arabian hotspot by S receiver functions, *Geophys. Res. Lett.,* **31,** L11608, doi:10.1029/2004GL019574.

Wang, R., 1999. A simple orthonormalization method for the stable and efficient computation of Green's functions, *Bull. seism. Soc. Am.,* **89,** 733–741.

Weber, M., 1988. Computation of body-wave seismograms in absorbing 2-D media using the Gaussian beam method: comparison with exact methods, *Geophys. J.,* **92,** 9–24.

Yuan, X., Ni, J., Kind, R., Mechie, J. & Sandvol, E., 1997. Lithospheric and upper mantle structure of southern Tibet from a seismological passive source experiment, *J. geophys. Res.,* **102,** 27 491–27 500.